

1 **Revision 1**

2 **Pressure-induced velocity softening in natural orthopyroxene at mantle temperature**

3

4 Siheng Wang^{1,*}, Ting Chen¹, Nao Cai², Xintong Qi¹, Adrian Fiege³, Robert C. Liebermann^{1,2},

5 Baosheng Li^{1,2}

6

7 ¹Department of Geosciences, Stony Brook University, Stony Brook, NY 11794, USA

8 ²Mineral Physics Institute, Stony Brook University, Stony Brook, NY 11794, USA

9 ³Department of Earth and Planetary Sciences, American Museum of Natural History, New York,
10 NY 10024, USA

11

12 *Corresponding author: Siheng Wang (siheng.wang@stonybrook.edu), Department of

13 Geosciences, Stony Brook University, Stony Brook, NY 11794, USA

14 **Abstract**

15 In this study, we have measured the compressional and shear wave velocities of
16 $(\text{Mg}_{1.77}\text{Fe}_{0.22}\text{Ca}_{0.01})\text{Si}_2\text{O}_6$ natural orthopyroxene up to 13.5 GPa and 873 K using ultrasonic
17 interferometry in conjunction with in-situ synchrotron X-ray diffraction and imaging techniques.
18 Previous acoustic experiments on orthoenstatite (OEn) MgSiO_3 indicated that both
19 compressional and shear velocities (V_P and V_S) of OEn undergo continuous velocity softening
20 above 9 GPa at room temperature, which has been attributed to the phase transition from OEn to
21 the metastable, high-pressure clinoenstatite HPCEn2. For the first time, our results suggest that
22 pressure-induced velocity softening can occur in natural orthopyroxene at high temperature
23 conditions relevant to the Earth's cold subduction zones. Estimates of the impedance and
24 velocity contrasts between orthopyroxene (Opx) and high-pressure clinopyroxene (HPCpx) have
25 been calculated, and the possibility of this phase transformation being a plausible candidate for
26 seismic X-discontinuities at depth around 250-350 km is re-evaluated.

27

28 **Key words:** Orthopyroxene; Velocity softening; High pressure and high temperature; Ultrasonic
29 interferometry.

30 **Introduction**

31 Orthopyroxene (Mg,FeSiO_3) is one of the most abundant minerals in the pyrolite
32 compositional model of Earth's upper mantle (Ringwood 1975). Several polymorphs of pure Mg
33 end-member enstatite (MgSiO_3) are thermodynamically stable under the pressure (P) and
34 temperature (T) conditions of the upper mantle (see Fig. 1), including orthoenstatite [OEn, space
35 group (SG): *Pbca*], protoenstatite (PEn, SG: *Pbcn*), low-pressure clinoenstatite (LPCEn, SG:
36 *P2₁/c*), and high-pressure clinoenstatite (HPCEn, SG: *C2/c*) (Gasparik 1990; Pacalo and
37 Gasparik 1990). Recently, a metastable, high-pressure monoclinic polymorph with space group
38 *P2₁/c* (designated as HPCEn2) has been discovered and reported to be persistent at least up to
39 673 K (J. Zhang et al. 2012; J. Zhang et al. 2014). Given the abundance of pyroxene in the
40 Earth's upper mantle, investigating the phase transformation behavior and physical properties of
41 pyroxene-structured groups has attracted the attention of many research groups (e.g., Angel and
42 Hugh-Jones 1994; Angel and Jackson 2002; Finkelstein et al. 2015; Frisillo and Barsch 1972;
43 Hugh-Jones and Angel 1997; Jackson et al. 2004; Jahn 2008; Kung et al. 2006; Lin 2003; Xu et
44 al. 2018; J. Zhang et al. 2012; Zhao et al. 1995).

45 Kung et al. (2004) observed a substantial softening of both the compressional and shear
46 velocities (V_P and V_S) in OEn above 9 GPa at room temperature. Subsequent experimental and
47 computational investigations (Li et al. 2014; J. Zhang et al. 2014) suggest that the softening
48 behavior may be related to the phase transformation from OEn to the newly discovered
49 monoclinic phase HPCEn2 with space group *P2₁/c*. At room temperature or moderate high
50 temperature, due to the reconstructive nature of the phase transition from OEn to HPCEn [which
51 requires reorientation of the stacked layers], the phase transformation is always kinetically
52 inhibited by energy barriers (Dera et al. 2013; J. Zhang et al. 2014); see black dotted line below

53 700K in Fig. 1. Thus, OEn would transform to the metastable phase HPCEn2. A recent study has
54 shown this metastable phase transition could occur at high temperatures up to 700 K (Xu et al.
55 2018). The velocity softening observed in MgSiO₃, at around 9 GPa, has also been observed in
56 FeSiO₃-orthoferrosilite at room temperature at ~5 GPa (see Kung and Li 2014). However, prior
57 to the current study, no attempt has ever been made to experimentally investigate if this pressure-
58 induced velocity softening can persist at high temperature. Li et al. (2014) speculate that if such a
59 softening behavior occurs at high temperatures in natural orthopyroxene compositions, the
60 velocity and impedance contrasts between Opx and HPCpx at mantle depths would be enhanced,
61 which could, in turn, increase their detectability in seismic studies.

62 The phase transition from Opx to HPCpx has been proposed to explain the seismic X-
63 discontinuity (e.g., Revenaugh and Jordan 1991; Woodland and Angel 1997) for a long time
64 because the transition pressure from Opx to HPCpx is well consistent with the depth of the
65 seismic discontinuity (Angel et al. 1992) and the phase transition boundary is sharp enough to
66 generate the discontinuity (Woodland 1998). Previous acoustic studies on Opx have been
67 conducted at high temperature and ambient pressure (e.g., Jackson et al. 2007; Kung et al. 2011)
68 or at room temperature and high pressure (e.g., Chai et al. 1997; Flesch et al. 1998; Kung et al.
69 2004; D. Zhang et al. 2013; J. Zhang and Bass 2016). The high P-T experiments on Opx have all
70 been focused on the investigation of the phase relationships and equation of state (EOS) of
71 orthopyroxene (e.g., Akashi et al. 2009; Xu et al. 2018; J. Zhang et al. 2014; Zhao et al. 1995).
72 To our knowledge, no direct experimental measurements of the acoustic velocities of
73 orthopyroxene at simultaneous high P-T conditions have been reported. To help us better
74 understand the cause of X-discontinuity, such acoustic velocity data at high pressure and high
75 temperature are needed.

76 In this study, we have conducted sound velocity and density measurements on a natural
77 orthopyroxene sample at simultaneous high P-T conditions using ultrasonic interferometry in
78 conjunction with in-situ synchrotron X-ray diffraction and imaging techniques. The elastic bulk
79 and shear properties as a function of pressure along a 673 K isotherm were determined directly,
80 thereby allowing an investigation of pressure induced velocity softening in orthopyroxene at
81 temperatures relevant to the Earth's subduction zones.

82 **Experimental Methods**

83 The polycrystalline sample of orthopyroxene used in the ultrasonic experiment was hot-
84 pressed at 5 GPa and 1273 K for 1 hour in a 1000-ton uniaxial split-cylinder apparatus (USCA-
85 1000) in the High Pressure Laboratory at Stony Brook University using natural pyroxene powder
86 (purchased from Ward's Scientific Establishment) as the starting material. The hot-pressing
87 experiment followed a specific P-T path designed to obtain a crack-free, fine-grained, and
88 homogeneous pyroxene sample (more details in Gwanmesia and Liebermann 1992).

89 High-pressure ultrasonic interferometric experiments were performed up to 13.5 GPa and
90 873 K in a 1000-ton Kawai-type, multi-anvil apparatus (T-25) in conjunction with synchrotron
91 X-radiation at beamline 13-ID-D of GSECARS of the Advanced Photon Source, Argonne
92 National Laboratory. Details of the experimental setup can be found elsewhere (Li and
93 Liebermann 2014) and a sketch up of the cell assembly is shown in Figure S1 in the
94 supplementary material. A dual mode LiNbO₃ transducer was used to generate and receive both
95 the compressional (P) wave and shear (S) wave simultaneously (50 MHz resonant frequency for
96 P wave and 30 MHz for S wave). The temperature was measured using W/Re3%-W/Re25%
97 thermocouple wires, with the junction immediately next to the sample near the center of the cell.
98 A dense alumina rod was placed on the top of the sample and served as the acoustic buffer rod.

99 Two thin pieces of gold foil (2 μm thickness) were put at the top and bottom of the sample
100 respectively to enhance the mechanical coupling and signal propagation, as well as serving as a
101 delineation of the sample's boundaries in X-radiography images. A disk of NaCl placed at the
102 back of the sample provided pseudo-hydrostatic environment for the sample, which also used as
103 an internal pressure marker using the equation of state from Decker (1971).

104 The experimental P-T path for the acoustic experiment is shown in Figure 1. X-ray
105 diffraction patterns of NaCl and the Opx sample, as well as the P and S wave travel times and
106 images of the sample were collected at a series of pressure and temperature conditions along the
107 designated P-T path. The initial compression to 3 GPa was performed at room temperature,
108 followed by heating to 473 K and further compression to 5 GPa. After heating the sample to 673
109 K at 5 GPa, pressure was increased up to 13.5 GPa along the 673 K isotherm, during which the
110 X-ray diffraction data of the sample were monitored closely by comparing with the standard
111 spectra of orthopyroxene (Opx, SG: *Pbca*) phase. At the peak pressure, the temperature was
112 increased to 873 K while the ram load was kept constant. Due to the relaxation of the pressure
113 medium, the pressure was found to have slightly decreased to 13.1 GPa and the sample was
114 transforming to high-pressure clinopyroxene (HPCpx, SG: *C2/c*, solid circles in Fig. 1, more
115 details in Results). An isothermal decompression along 873 K was then performed and data for
116 HPCpx were collected as pressure was slowly decreased to 9.9 GPa.

117 X-ray diffraction patterns were collected in energy dispersive mode at fixed 2θ (6.10°). The
118 recorded diffraction patterns from the sample were analyzed using the Le Bail method with the
119 GSAS/EXPGUI program (Larson and Von Dreele 1994; Toby 2001) to derive the lattice
120 parameters and thus densities (see Figure S2 in supplementary material). The measured cell
121 parameters of NaCl were used to determine the cell pressures using the equation of state of

122 Decker's implemented in PDindexer software (Seto et al. 2010). The maximum uncertainty in
123 the calculated pressure is ~ 0.4 GPa (Decker 1965, 1971). P and S wave travel times were
124 obtained by the pulse echo overlap (PEO) method, which has been described elsewhere (Li et al.
125 2002; Li et al. 2004). The error for travel times is about 0.2 ns. The bond perturbations
126 contributed by the gold foils to travel time for Opx (0.7 ns for P waves and -0.7 ns for S waves)
127 and HPCpx (0.8 ns for P waves and -1.0 ns for S waves) were corrected following the procedures
128 of Niesler and Jackson (1989). Sample lengths were obtained from the X-radiography images
129 recorded by the CCD camera, with a precision within 0.25%. The length of the recovered sample
130 measured after high pressure run is $L_0 = 0.987(1)$ mm.

131 Scanning Electron Microscope (SEM) analysis was conducted on the recovered sample at
132 Geodynamic Research Center, Ehime University, Japan. The results (Fig. 2) indicate that the
133 sample is homogenous with average grain size less than 10 microns. Part of the final recovered
134 sample was used for chemical analysis by using a 5-spectrometer Cameca SX-100 electron
135 microprobe at American Museum of Natural History. All elemental analyses were performed at
136 an accelerating voltage of 15 kV, a beam current of 20 nA, and using a beam size of 1 μm . We
137 measured Si (calibrated on diopside), Fe (fayalite), Mg (diopside), Ca (diopside). The counting
138 time was 20 s for all elements. The composition of this natural sample was determined to be
139 $(\text{Mg}_{1.77}\text{Fe}_{0.22}\text{Ca}_{0.01})\text{Si}_2\text{O}_6$.

140 **Results**

141 Travel times in the current sample were measured as a function of pressure along both 673 K
142 and 873 K isotherms. As shown in Fig. 3a, P wave travel times decreased monotonically with
143 increasing pressure, with a rapid reduction in the rate of change with pressure from $\sim 5 \times 10^{-2}$
144 s/GPa at 5 GPa to $\sim 5 \times 10^{-3}$ s/GPa at 13.5 GPa. While for S waves shown in Fig. 3b, the travel

145 times decreased with increasing pressure up to ~11 GPa and then became independent of
146 pressure within 11-11.8 GPa; above 11.8 GPa, the S wave travel times begin to increase as
147 pressure was increased to 13.5 GPa. In their study of MgSiO₃, Kung et al. (2004) reported that
148 both P and S wave travel times decreased up to 9 GPa, then started to increase up to ~13 GPa.
149 Similar anomalies have also been observed within 5-7 GPa in a the study on FeSiO₃ ferrosilite
150 (see Fig. 4 in Kung and Li 2014). These anomalies have been interpreted as precursors to the
151 transition to the metastable HPCEn2 phase (Kung and Li 2014; Li et al. 2014). Taking into
152 account the different composition as well as temperature [(Mg_{1.77}Fe_{0.22}Ca_{0.01})Si₂O₆ and 673 K]
153 compared with those at room temperature for MgSiO₃ and FeSiO₃, the observed travel times in
154 this study, especially for S waves, are consistent with those in previous studies, suggesting that
155 the anomalous travel time-pressure behavior can be sustained at 673 K in Opx with magnesium-
156 rich compositions. Fig. 3c shows the length changes of the sample as a function of pressure and
157 temperature obtained using X-radiography images. The lengths of the Opx sample decreased
158 with increasing pressure up to 13.5 GPa in a nearly linear manner; no anomalous behavior was
159 observed. Thus, the anomalous behavior of the acoustic travel times in Fig. 3 a and b is solely
160 due to changes in the intrinsic elastic properties of orthopyroxene.

161 X-ray diffraction patterns are shown in Fig. 4. After cold compression to 5.0 GPa and heating
162 to 673 K, orthopyroxene (Opx, SG: *Pbca*) remains the single phase of the sample (Fig. 4 a and b).
163 During the subsequent compression along 673 K, although the travel times exhibit anomalous
164 behavior after 11.0 GPa, the X-ray diffraction patterns collected from 11.0 GPa to 13.5 GPa (Fig.
165 4c) did not change dramatically nor exhibit extra peaks, continuing to exhibit the strong
166 fingerprint of Opx. The values of χ^2 (a measure of the goodness of fit) from fitting to single Opx
167 (SG: *Pbca*) phase remain in a low level ($\chi^2 < 4$). According to a previous study by J. Zhang et al.

168 (2012) on a natural Fe-bearing orthopyroxene ($\text{Mg}_{1.74}\text{Fe}_{0.16}\text{Al}_{0.05}\text{Ca}_{0.04}\text{Cr}_{0.01}$)($\text{Si}_{1.94}\text{Al}_{0.06}$) O_6 , the
169 phase transition from Opx to HPCpx2 occurred at 14.26 GPa on compression at room
170 temperature. J. Zhang et al. (2014) also reported two transition pressures for natural samples
171 (14.5 GPa for near end-member Mg Opx; 13.3 GPa for Al + Fe-bearing Opx) at high temperature
172 of 673 K. It is likely that in the current experiments the Opx (SG: *Pbca*) phase did not transform
173 to HPCpx (SG: *P2₁/c*) at the maximum pressure of 13.5 GPa.

174 After heating to 873 K, clear changes were identified in the X-ray diffraction pattern (Fig.
175 4d), indicative of the phase transformation from Opx (*Pbca*) to HPCpx (*C2/c*). However, based
176 on the travel times and the X-ray diffraction pattern at 13.1 GPa 873 K, it is hard to evaluate
177 whether a complete transformation occurred or not because many peaks of HPCpx overlap with
178 those of Opx. Thus, it is likely that the sample at 13.1 GPa, 873 K consists mostly HPCpx with a
179 small amount of Opx. Due to the resolution limit of the current energy dispersive data, however,
180 the proportions of Opx (*Pbca*) and HPCpx (*C2/c*) could not be determined. On further
181 decompression below 9.9 GPa, the acoustic signal was lost. The recovered phase was low-
182 pressure clinopyroxene LPCpx (*P2₁/c*), which was not observed during compression, confirming
183 the full conversion to the HPCpx (*C2/c*) phase at 873 K before it was quenched to ambient
184 condition.

185 Discussion

186 P and S wave velocities of the natural pyroxene are calculated by $V_{(P, S)} = 2L/T_{(P, S)}$ and
187 plotted as a function of pressure in Figure 5. The results are compared to published P and S wave
188 velocities measured in Mg end-member orthoenstatite and Fe end-member orthoferrosilite by
189 using ultrasonic interferometry at room temperature, as well as to published data for synthetic
190 Fe-bearing Opx ($\text{Mg}_{0.87}\text{Fe}_{0.13}$) Si_2O_6 derived from nuclear resonant inelastic X-ray scattering,

191 NRIXS (Kung and Li 2014; Kung et al. 2004; D. Zhang et al. 2013). At room temperature,
192 pressure-induced velocity softening has been observed for the Mg end-member, the Fe end-
193 member, and the synthetic $\text{Mg}_2\text{Si}_2\text{O}_6$ - $\text{Fe}_2\text{Si}_2\text{O}_6$ solid solution. The P wave velocity of Opx in this
194 study increases steadily with pressure and decreases slightly at ~ 13 GPa, while the S wave
195 velocity exhibits a pronounced velocity softening above 11 GPa, reaching $\sim 1.6\%$ at ~ 13.5 GPa.
196 Stronger S wave softening than P wave was also observed in the Fe end-member ferrosilite
197 experiment (see orange pentagons in Fig. 5, in which the solid pentagons are for compression
198 while open pentagons are for decompression). These data for ferrosilite indicate that this could
199 be due to the presence of iron in the structure, which greatly reduces the shear elastic stiffness
200 coefficients under pressure, especially C_{44} , C_{55} , and C_{66} (Kung and Li 2014; D. Zhang et al.
201 2013). Similar behavior was observed in synthetic Fe-bearing Opx using NRIXS (D. Zhang et al.
202 2013). In that study, only the Debye sound velocity was obtained directly, and then V_P and V_S
203 were calculated using density and bulk modulus data from a separate P-V-T experiment. In their
204 experiment, D. Zhang et al. (2013) used the Opx (SG: *Pbca*) EOS to fit the data up to 10.5 GPa
205 and the HPCpx2 (SG: $P2_1/c$) EOS to fit the data at 12.3 GPa and 17 GPa. Thus, the velocity
206 softening is caused by the structure changes in two different phases. But from our XRD results,
207 the velocity softening occurs within a single phase with the *Pbca* symmetry. Therefore, the
208 elastic softening of enstatite-rich pyroxene cannot be properly evaluated unless simultaneous
209 measurements of acoustic velocity and X-ray diffraction for phase characterization are available.

210 The compression mechanism of Opx may be described by the rotation and kinking of SiO_4
211 tetrahedral chains and distortions of MgO_6 octahedra (see Fig. 3 in Li et al. 2014). Both the Si-O
212 and Mg-O bond lengths show monotonic decreases as a function of pressure, while the A-site
213 SiO_4 tetrahedral chain angles θ_A , which was reported to be highly correlated with C_{55} , do not

214 exhibit monotonic behavior with pressure (Li et al. 2014). The trend change in O3A-O3A-O3A
215 chain angle suggests a weakening restoring force which may be due to the increased kinking of
216 silicon tetrahedral chains. As shown in Fig. 5, larger velocity softening for S waves than that for
217 P waves has been observed in all three cases with different compositions and/or at different
218 temperatures, which could be interpreted using the relationship between elastic moduli (K_S , G)
219 and velocities ($V_P = \sqrt{(K_S + \frac{4}{3}G)/\rho}$, $V_S = \sqrt{G/\rho}$). Thus, the decrease of both P and S wave
220 velocities in Opx could be largely due to the softening in shear modulus G , which is
221 predominantly caused by the softening of the shear elastic constant C_{55} with increasing pressure
222 as reported by previous density functional theory calculations of Li et al. (2014) and Qian et al.
223 (2018).

224 Compared to pure Mg-end member and Fe-end member studies, the softening behavior of the
225 natural sample at high temperature starts at a higher pressure, which may indicate a positive
226 dP/dT slope of the phase boundary between Opx and HPCpx2. At higher temperature, the phase
227 transition of Opx to HPCpx2 would occur at higher pressure. The elastic moduli K_S and G as a
228 function of pressure at 673 K are plotted in Fig. 6. The propagated uncertainties in the bulk and
229 shear moduli are approximately 0.5%. The shear modulus increases to about 11 GPa, then
230 decreases slightly, which also serves as a precursor to the pressure-induced phase transition from
231 $Pbca$ into $P2_1/c$ structure from 12 to 14 GPa as observed in Raman data for Opx (J. Zhang et al.
232 2012; J. Zhang et al. 2014).

233 **Implications**

234 Based on the current study, Opx (SG: $Pbca$) with Mg-rich composition transforms into
235 HPCpx (SG: $C2/c$) when the temperature is increased from 673 to 873 K at ~13 GPa, providing

236 an upper bound in temperature at which Opx can be preserved at high pressures. Considering the
237 geotherm of cold slabs shown in Fig. 1, when $T < 873$ K the Opx may experience softening
238 before its transformation to HPCpx, lowering the seismic velocity of the subducting slab as well
239 as increasing the seismic velocity contrast at the phase transition to HPCpx. In addition, previous
240 studies on the compositional effects on the phase transition of Opx (*Pbca*) to HPCpx2 (*P2₁/c*)
241 show that 10 mol% Fe content could decrease the onset pressure of the initial formation of
242 HPCpx2 by ~ 1 GPa while a small amount of Al and Ca (0.212 pfu and 0.032 pfu, respectively)
243 would increase the pressure by over 3 GPa (J. Zhang et al. 2013). Thus, in regions where the
244 composition of Opx is the Al-free, Ca-free and Fe-rich, there is a possibility the velocity
245 softening behavior of Opx can occur at shallower depth in the subduction zones.

246 Seismic X-discontinuities at 250-350 km depths with a positive shear impedance (ρV_S)
247 contrast (3-8%) in the upper mantle have been observed in many seismic studies (e.g., Deuss and
248 Woodhouse 2002; Deuss and Woodhouse 2004; Revenaugh and Jordan 1991; Schmerr et al.
249 2013; Zhang and Lay 1993). The phase transformation of Opx (*Pbca*) to HPCpx (*C2/c*) has been
250 proposed to be one of the plausible candidates for the cause of X-discontinuity. The shear
251 impedance contrast caused by this phase transition has been estimated to be only around 1% (e.g.,
252 Woodland 1998; Woodland and Angel 1997; D. Zhang et al. 2013), which is relatively small
253 compared to seismological observations. However, based on extant studies (this study; Kung and
254 Li 2014; Kung et al. 2004), the pressure-induced velocity softening behavior is a characteristic
255 property of the Opx (*Pbca*) phase at least up to 673K, regardless of whether the transformation is
256 to HPCpx (*C2/c*) or the metastable phase HPCpx2 (*P2₁/c*). Thus, the shear impedance contrast of
257 Opx-HPCpx would be enhanced in the pressure range where the softening behavior occurs. Here,
258 we provide the direct information of the elasticity of both Opx and HPCpx phases at high

259 temperatures in a same experiment. Thermal effects of K_S and G were corrected from the data at
260 3.1 GPa in this experiment for Opx and the results from Kung et al. (2005) for HPCpx. Along the
261 cold subduction slab geotherm shown in Fig. 1, the density jumps at a pressure range of ~10-12
262 GPa is about 2.4%, associating with the shear velocity jumps of 5.7-6.3% and shear impedance
263 contrasts of 8.0-8.4%. The impedance contrasts here are defined by:
264
$$C = \frac{\rho_{\text{HPCpx}} V_{\text{HPCpx}} - \rho_{\text{Opx}} V_{\text{Opx}}}{\frac{1}{2}(\rho_{\text{HPCpx}} V_{\text{HPCpx}} + \rho_{\text{Opx}} V_{\text{Opx}})} \times 100\%$$
. Considering the abundance of Opx in the Earth's
265 interior, the estimation of shear impedance contrast is about 0.8-1.7% in the pyrolitic
266 composition and up to 3.4% in some pyroxene-enriched regions (Irfune and Ringwood 1987;
267 Ringwood 1975, 1991), comparable to those seismic observations for the X-discontinuity. In Fe-
268 rich subduction zones where the softening behavior should occur at shallower depth, the
269 impedance contrast caused by the phase transition of Opx (*Pbca*) to HPCpx (*C2/c*) would be
270 even larger than previously estimated. Therefore, the Opx-HPCpx phase transition could still be
271 one of the contributing factors for the seismic X-discontinuity, especially in the pyroxene rich
272 area along the cold subducted slabs.

273 **Acknowledgements**

274 The authors would like to thank Yanbin Wang and Tony Yu for help in conducting the ultrasonic
275 experiment at the Advanced Photon Source and David Welch for valuable discussions. Ting
276 Chen thanks the Geodynamic Research Center (Ehime University, Japan) for a summer
277 internship, during which the SEM analysis was done. This project is supported by National
278 Science Foundation (EAR-1524078) and DOE-NNSA (DE-NA0002907). GeoSoilEnviroCARS
279 is supported by the National Science Foundation - Earth Sciences (EAR-1634415) and
280 Department of Energy-GeoSciences (DE-FG02-94ER14466). This research used resources of the

281 Advanced Photon Source, a U.S. Department of Energy (DOE) Office of Science User Facility
282 operated for the DOE Office of Science by Argonne National Laboratory under Contract No.
283 DE-AC02-06CH11357. MPI publication number 510.

284 **References cited**

- 285 Akashi, A., Nishihara, Y., Takahashi, E., Nakajima, Y., Tange, Y., and Funakoshi, K.i. (2009)
286 Orthoenstatite/clinoenstatite phase transformation in MgSiO₃ at high-pressure and high-
287 temperature determined by in situ X-ray diffraction: Implications for nature of the X
288 discontinuity. *Journal of Geophysical Research*, 114, B04206.
- 289 Angel, R.J., Chopelas, A., and Ross, N.L. (1992) Stability of High-Density Clinoenstatite at
290 Upper-Mantle Pressures. *Nature*, 358(6384), 322-324.
- 291 Angel, R.J., and Hugh-Jones, D.A. (1994) Equations of state and thermodynamic properties of
292 enstatite pyroxenes. *Journal of Geophysical Research: Solid Earth*, 99(B10), 19777-
293 19783.
- 294 Angel, R.J., and Jackson, J.M. (2002) Elasticity and equation of state of orthoenstatite, MgSiO₃.
295 *American Mineralogist*, 87(4), 558-561.
- 296 Chai, M., Brown, J.M., and Slutsky, L.J. (1997) The elastic constants of an aluminous
297 orthopyroxene to 12.5 GPa. *Journal of Geophysical Research: Solid Earth*, 102(B7),
298 14779-14785.
- 299 Decker, D.L. (1965) Equation of State of NaCl and its Use as a Pressure Gauge in High-Pressure
300 Research. *Journal of Applied Physics*, 36(1), 157-161.
- 301 Decker, D.L. (1971) High-Pressure Equation of State for NaCl, KCl, and CsCl. *Journal of*
302 *Applied Physics*, 42(8), 3239-3244.
- 303 Dera, P., Finkelstein, G.J., Duffy, T.S., Downs, R.T., Meng, Y., Prakapenka, V., and Tkachev, S.
304 (2013) Metastable high-pressure transformations of orthoferrosilite Fs(82). *Physics of the*
305 *Earth and Planetary Interiors*, 221, 15-21.
- 306 Deuss, A., and Woodhouse, J.H. (2002) A systematic search for mantle discontinuities using SS-
307 precursors. *Geophysical Research Letters*, 29(8), 90-1-90-4.
- 308 Deuss, A., and Woodhouse, J.H. (2004) The nature of the Lehmann discontinuity from its
309 seismological Clapeyron slopes. *Earth and Planetary Science Letters*, 225(3-4), 295-304.
- 310 Finkelstein, G.J., Dera, P.K., and Duffy, T.S. (2015) Phase transitions in orthopyroxene (En₉₀) to
311 49 GPa from single-crystal X-ray diffraction. *Physics of the Earth and Planetary Interiors*,
312 244, 78-86.
- 313 Flesch, L.M., Li, B., and Liebermann, R.C. (1998) Sound velocities of polycrystalline MgSiO₃-
314 orthopyroxene to 10 GPa at room temperature. *American Mineralogist*, 83(5-6), 444-450.
- 315 Frisillo, A.L., and Barsch, G.R. (1972) Measurement of Single-Crystal Elastic-Constants of
316 Bronzite as a Function of Pressure and Temperature. *Journal of Geophysical Research*,
317 77(32), 6360-6384.
- 318 Gasparik, T. (1990) A Thermodynamic Model for the Enstatite-Diopside Join. *American*
319 *Mineralogist*, 75(9-10), 1080-1091.

- 320 Gwanmesia, G.D., and Liebermann, R.C. (1992) Polycrystals of high-pressure phases of mantle
321 minerals: Hot-pressing and characterization of physical properties. High-pressure
322 research: Application to Earth and planetary sciences ed. by Y. Syono and M. H.
323 Manghnani, pp 117-135, Terra Scientific Publishing Co., Tokyo/American Geophysical
324 Union, Washington, D. C., 1992.
- 325 Hugh-Jones, D.A., and Angel, R.J. (1997) Effect of Ca^{2+} and Fe^{2+} on the equation of state of
326 MgSiO_3 orthopyroxene. *Journal of Geophysical Research-Solid Earth*, 102(B6), 12333-
327 12340.
- 328 Irifune, T., and Ringwood, A.E. (1987) Phase-Transformations in a Harzburgite Composition to
329 26 Gpa - Implications for Dynamical Behavior of the Subducting Slab. *Earth and*
330 *Planetary Science Letters*, 86(2-4), 365-376.
- 331 Jackson, J.M., Sinogeikin, S.V., and Bass, J.D. (2007) Sound velocities and single-crystal
332 elasticity of orthoenstatite to 1073 K at ambient pressure. *Physics of the Earth and*
333 *Planetary Interiors*, 161(1-2), 1-12.
- 334 Jackson, J.M., Sinogeikin, S.V., Carpenter, M.A., and Bass, J.D. (2004) Novel phase transition in
335 orthoenstatite. *American Mineralogist*, 89(1), 239-244.
- 336 Jahn, S. (2008) High-pressure phase transitions in MgSiO_3 orthoenstatite studied by atomistic
337 computer simulation. *American Mineralogist*, 93(4), 528-532.
- 338 Kirby, S.H., Stein, S., Okal, E.A., and Rubie, D.C. (1996) Metastable mantle phase
339 transformations and deep earthquakes in subducting oceanic lithosphere. *Reviews of*
340 *Geophysics*, 34(2), 261-306.
- 341 Kung, J., Jackson, I., and Liebermann, R.C. (2011) High-temperature elasticity of polycrystalline
342 orthoenstatite (MgSiO_3). *American Mineralogist*, 96(4), 577-585.
- 343 Kung, J., and Li, B. (2014) Lattice Dynamic Behavior of Orthoferrosilite (FeSiO_3) toward Phase
344 Transition under Compression. *The Journal of Physical Chemistry C*, 118(23), 12410-
345 12419.
- 346 Kung, J., Li, B., and Liebermann, R.C. (2006) Ultrasonic observations of elasticity changes
347 across phase transformations in MgSiO_3 pyroxenes. *Journal of Physics and Chemistry of*
348 *Solids*, 67(9-10), 2051-2055.
- 349 Kung, J., Li, B., Uchida, T., and Wang, Y. (2005) In-situ elasticity measurement for the
350 unquenchable high-pressure clinopyroxene phase: Implication for the upper mantle.
351 *Geophysical Research Letters*, 32, L01307.
- 352 Kung, J., Li, B., Uchida, T., Wang, Y., Neuville, D., and Liebermann, R.C. (2004) In situ
353 measurements of sound velocities and densities across the orthopyroxene \rightarrow high-pressure
354 clinopyroxene transition in MgSiO_3 at high pressure. *Physics of the Earth and Planetary*
355 *Interiors*, 147(1), 27-44.
- 356 Larson, A.C., and Von Dreele, R.B. (1994) GSAS. Report IAU, 86-748.
- 357 Li, B., Chen, K., Kung, J., Liebermann, R.C., and Weidner, D.J. (2002) Sound velocity
358 measurement using transfer function method. *Journal of Physics-Condensed Matter*,
359 14(44), 11337-11342.
- 360 Li, B., Kung, J., and Liebermann, R.C. (2004) Modern techniques in measuring elasticity of
361 Earth materials at high pressure and high temperature using ultrasonic interferometry in
362 conjunction with synchrotron X-radiation in multi-anvil apparatus. *Physics of the Earth*
363 *and Planetary Interiors*, 143, 559-574.

- 364 Li, B., Kung, J., Liu, W., and Liebermann, R.C. (2014) Phase transition and elasticity of enstatite
365 under pressure from experiments and first-principles studies. *Physics of the Earth and*
366 *Planetary Interiors*, 228, 63-74.
- 367 Li, B., and Liebermann, R.C. (2014) Study of the Earth's interior using measurements of sound
368 velocities in minerals by ultrasonic interferometry. *Physics of the Earth and Planetary*
369 *Interiors*, 233, 135-153.
- 370 Lin, C.-C. (2003) Pressure-induced metastable phase transition in orthoenstatite (MgSiO_3) at
371 room temperature: a Raman spectroscopic study. *Journal of Solid State Chemistry*,
372 174(2), 403-411.
- 373 Niesler, H., and Jackson, I. (1989) Pressure Derivatives of Elastic Wave Velocities from
374 Ultrasonic Interferometric Measurements on Jacketed Polycrystals. *Journal of the*
375 *Acoustical Society of America*, 86(4), 1573-1585.
- 376 Pacalo, R.E.G., and Gasparik, T. (1990) Reversals of the Orthoenstatite-Clinoenstatite Transition
377 at High-Pressures and High-Temperatures. *Journal of Geophysical Research-Solid Earth*
378 *and Planets*, 95(B10), 15853-15858.
- 379 Qian, W., Wang, W., Zou, F., and Wu, Z. (2018) Elasticity of Orthoenstatite at High Pressure
380 and Temperature: Implications for the Origin of Low V_p/V_s Zones in the Mantle Wedge.
381 *Geophysical Research Letters*, 45(2), 665-673.
- 382 Revenaugh, J., and Jordan, T.H. (1991) Mantle layering from ScS reverberations: 3. The upper
383 mantle. *Journal of Geophysical Research: Solid Earth*, 96(B12), 19781-19810.
- 384 Ringwood, A.E. (1975) *Composition and petrology of the earth's mantle*. xvi, 618 p. p. McGraw-
385 Hill, New York,.
- 386 Ringwood, A.E. (1991) Phase-Transformations and Their Bearing on the Constitution and
387 Dynamics of the Mantle. *Geochimica Et Cosmochimica Acta*, 55(8), 2083-2110.
- 388 Schmerr, N.C., Kelly, B.M., and Thorne, M.S. (2013) Broadband array observations of the
389 300 km seismic discontinuity. *Geophysical Research Letters*, 40(5), 841-846.
- 390 Seto, Y., Nishio-Hamane, D., Nagai, T., and Sata, N. (2010) Development of a Software Suite on
391 X-ray Diffraction Experiments. *The Review of High Pressure Science and Technology*,
392 20, 269-276.
- 393 Toby, B.H. (2001) EXPGUI, a graphical user interface for GSAS. *Journal of Applied*
394 *Crystallography*, 34(2), 210-213.
- 395 Woodland, A.B. (1998) The orthorhombic to high-P monoclinic phase transition in Mg-Fe
396 Pyroxenes: Can it produce a seismic discontinuity? *Geophysical Research Letters*, 25(8),
397 1241-1244.
- 398 Woodland, A.B., and Angel, R.J. (1997) Reversal of the orthoferrosilite - high-P clinoferrosilite
399 transition, a phase diagram for FeSiO_3 and implications for the mineralogy of the Earth's
400 upper mantle. *European Journal of Mineralogy*, 9(2), 245-254.
- 401 Xu, J., Zhang, D., Fan, D., Zhang, J.S., Hu, Y., Guo, X., Dera, P., and Zhou, W. (2018) Phase
402 Transitions in Orthoenstatite and Subduction Zone Dynamics: Effects of Water and
403 Transition Metal Ions. *Journal of Geophysical Research: Solid Earth*, 123(4), 2723-2737.
- 404 Zhang, D., Jackson, J.M., Chen, B., Sturhahn, W., Zhao, J., Yan, J., and Caracas, R. (2013)
405 Elasticity and lattice dynamics of enstatite at high pressure. *Journal of Geophysical*
406 *Research: Solid Earth*, 118(8), 4071-4082.
- 407 Zhang, J.S., and Bass, J.D. (2016) Single-crystal elasticity of natural Fe-bearing orthoenstatite
408 across a high-pressure phase transition. *Geophysical Research Letters*, 43(16), 8473-8481.

- 409 Zhang, J.S., Dera, P., and Bass, J.D. (2012) A new high-pressure phase transition in natural Fe-
410 bearing orthoenstatite. *American Mineralogist*, 97(7), 1070-1074.
- 411 Zhang, J.S., Reynard, B., Montagnac, G., and Bass, J.D. (2014) Pressure-induced Pbc_a-P2₁/c
412 phase transition of natural orthoenstatite: The effect of high temperature and its
413 geophysical implications. *Physics of the Earth and Planetary Interiors*, 228, 150-159.
- 414 Zhang, J.S., Reynard, B., Montagnac, G., Wang, R.C., and Bass, J.D. (2013) Pressure-induced
415 Pbc_a-P2₁/c phase transition of natural orthoenstatite: Compositional effect and its
416 geophysical implications. *American Mineralogist*, 98(5-6), 986-992.
- 417 Zhang, Z., and Lay, T. (1993) Investigation of upper mantle discontinuities near Northwestern
418 Pacific Subduction Zones using precursors to sSH. *Journal of Geophysical Research:*
419 *Solid Earth*, 98(B3), 4389-4405.
- 420 Zhao, Y., Schiferl, D., and Shankland, T.J. (1995) A High P-T Single-Crystal X-Ray-Diffraction
421 Study of Thermoelasticity of MgSiO₃ Orthoenstatite. *Physics and Chemistry of Minerals*,
422 22(6), 393-398.
- 423

WANG ET AL.: P-INDUCED VELOCITY SOFTENING IN OPX AT MANTLE TEMPERATURE

424 **Table 1.** Elasticity properties of Fe-bearing natural orthopyroxene at high temperature and
 425 pressure.

	Pressure	T	Length	2tp	2ts	V _P	V _S	K _S	G	Volume	ρ
	(GPa)	(K)	(mm)	(μs)	(μs)	(km/s)	(km/s)	(GPa)	(GPa)	(Å ³)	(g/cm ³)
Opx	0	300								838.45(10)	3.295
Opx	0.9	300	0.993	0.2497	0.4175	7.96(2)	4.76(1)	109.9	75.2	831.87(9)	3.321
Opx	3.1	300	0.982	0.2335	0.4031	8.42(2)	4.87(1)	132.7	80.5	814.88(9)	3.390
Opx	3.1	473	0.984	0.2363	0.4083	8.33(2)	4.82(1)	129.6	78.5	817.54(11)	3.379
Opx	5.0	673	0.978	0.2269	0.3989	8.62(2)	4.90(1)	143.8	81.8	811.62(11)	3.404
Opx	6.5	673	0.973	0.2205	0.3918	8.82(2)	4.97(1)	154.4	84.7	804.71(11)	3.433
Opx	7.0	673	0.971	0.2187	0.3903	8.88(2)	4.98(1)	158.0	85.3	801.30(11)	3.447
Opx	8.1	673	0.967	0.2155	0.3873	8.98(2)	4.99(1)	164.5	86.7	794.65(10)	3.476
Opx	9.2	673	0.964	0.2131	0.3849	9.05(2)	5.01(1)	169.6	87.9	789.40(8)	3.499
Opx	10.0	673	0.963	0.2111	0.3835	9.12(2)	5.02(1)	174.7	88.8	784.09(8)	3.523
Opx	11.0	673	0.961	0.2095	0.3829	9.17(2)	5.02(1)	179.2	89.3	779.33(7)	3.545
Opx	11.8	673	0.959	0.2087	0.3829	9.19(2)	5.01(1)	181.6	89.3	775.59(8)	3.562
Opx	12.6	673	0.957	0.2081	0.3845	9.20(2)	4.98(1)	184.6	88.7	771.46(9)	3.581
Opx	13.5	673	0.954	0.2077	0.3871	9.19(2)	4.93(1)	187.2	87.5	767.94(9)	3.597
HPCpx*	13.1	873	0.945	0.2000	0.3662	9.45(2)	5.16(1)				
HPCpx	11.9	873	0.947	0.1986	0.3604	9.54(2)	5.26(1)	196.7	100.4	380.32(4)	3.632
HPCpx	9.9	873	0.951	0.2028	0.3630	9.38(2)	5.24(1)	184.7	98.8	384.04(4)	3.597
LPCpx	0	300	0.987								

426 Note*: a mixture phase of HPCpx and Opx

427

428 **FIG. 1.** Topology of the phase diagram for (Mg,Fe)SiO₃ and the pressure-temperature path in
429 the ultrasonic experiments presented in the study (lines with arrows and circles). Open circles:
430 orthopyroxene (Opx); Solid circles: high-pressure clinopyroxene (HPCpx). Solid lines: Phase
431 boundaries for MgSiO₃ (black, Gasparik 1990) and FeSiO₃ (blue, Woodland and Angel 1997).
432 Black dotted lines: Extrapolated phase boundaries below 700 K. Gray dash line: Cold slab
433 geotherm (Kirby et al. 1996). OEn = orthoenstatite; HPCEn = high-pressure clinoenstatite;
434 LPCEn = low-pressure clinoenstatite; PEn = protoenstatite; OFs = orthoferrosilite; HPCFs =
435 high-pressure clinoferrosilite; LPCFs = low-pressure clinoferrosilite; Wad = Wadsleyite; St =
436 stishovite; Rwd = ringwoodite.

437

438 **FIG. 2.** Scanning Electron Microscope (SEM) image of the recovered sample.

439

440 **FIG. 3.** (a) P wave and (b) S wave travel times of (Mg,Fe)SiO₃ as a function of pressure. The
441 error for travel times is about 0.2ns. (c) Length changes (L/L₀) in sample. The error for sample
442 length is about ±0.1%.

443

444 **FIG. 4.** X-ray diffraction patterns. (a) starting material with orthopyroxene structure (Pbca) at
445 ambient conditions; (b) after cold compression to 5.0 GPa, the sample was heated to 673 K; (c)
446 Opx after compressed to 13.5 GPa along 673 K; (d) HPCpx at 13.1 GPa after transforming from
447 orthopyroxene by heating to 873 K with minor amount of Opx (not indexed); (e) the final
448 recovered phase identified as low-pressure clinopyroxene (P2₁/c). Tickmarks in red indicate peak
449 positions for the NaCl pressure medium.

450

451 **FIG. 5.** P and S wave velocities of pyroxene as a function of pressure up to 13.5 GPa
452 determined by ultrasonic measurements in this study compared with previous results (see
453 Legend). UI: ultrasonic interferometry; NRIXS: nuclear resonant inelastic X-ray scattering.

454

455 **FIG. 6.** Adiabatic bulk (K_S) and shear (G) modulus for orthopyroxene as a function of pressure
456 up to 13.5 GPa at 673 K determined from the ultrasonic measurements (this study).

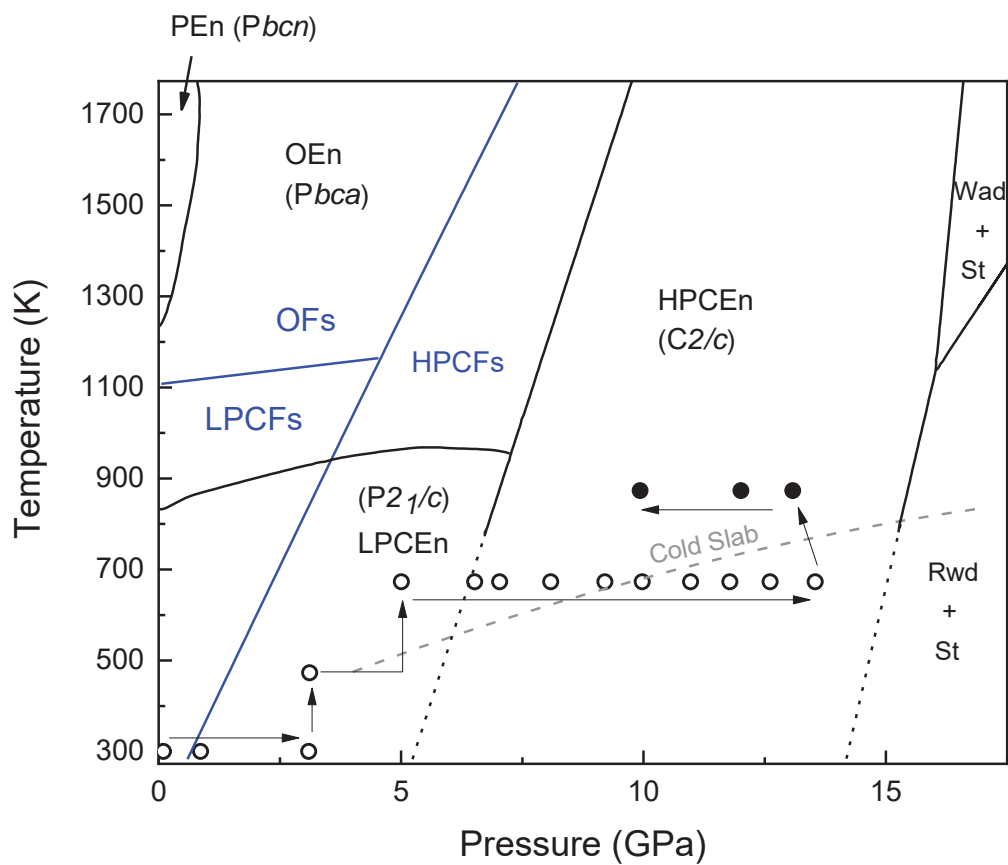


Figure 1

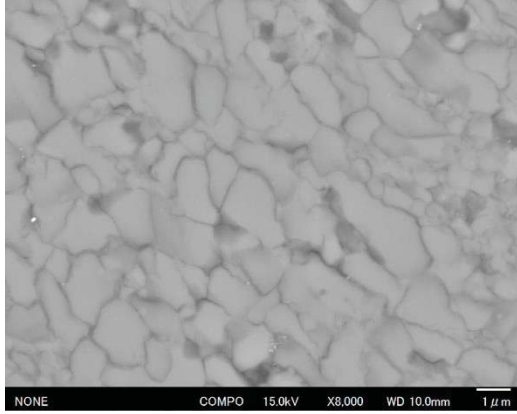


Figure 2

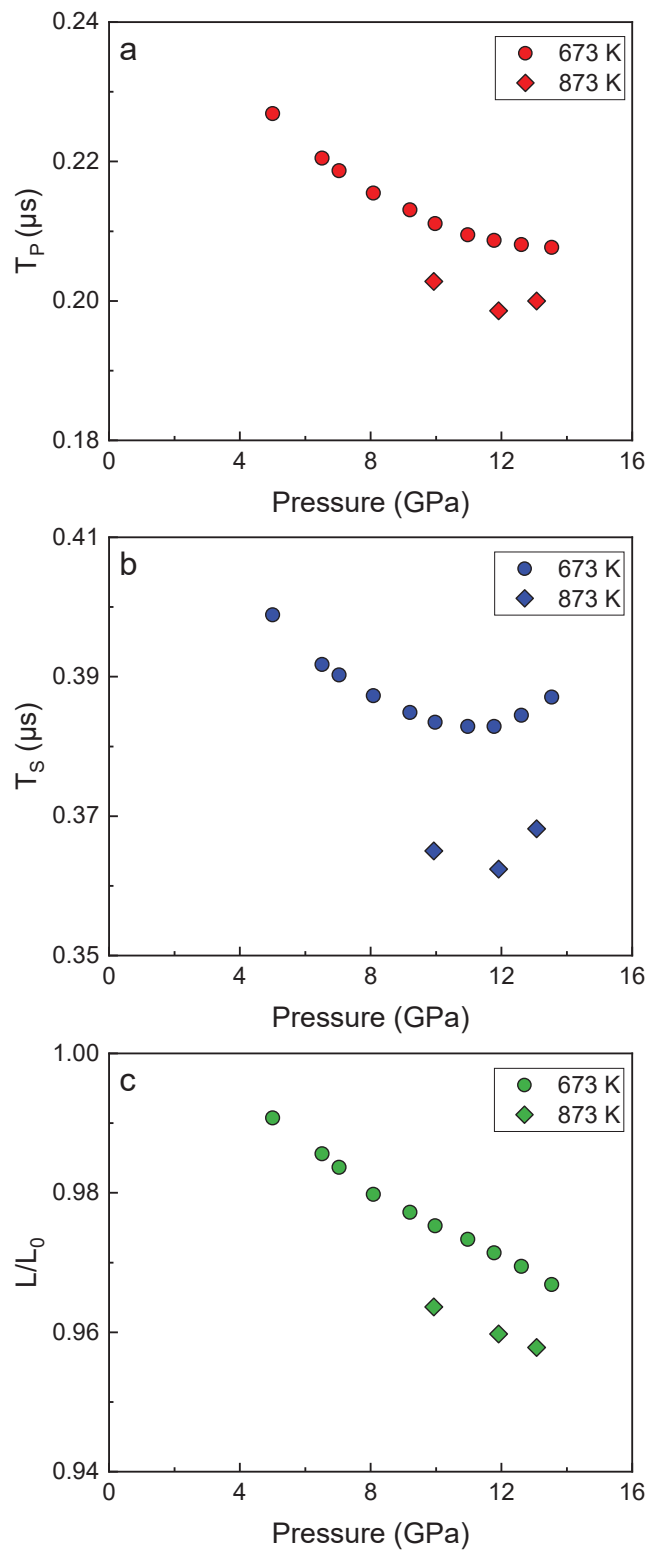


Figure 3

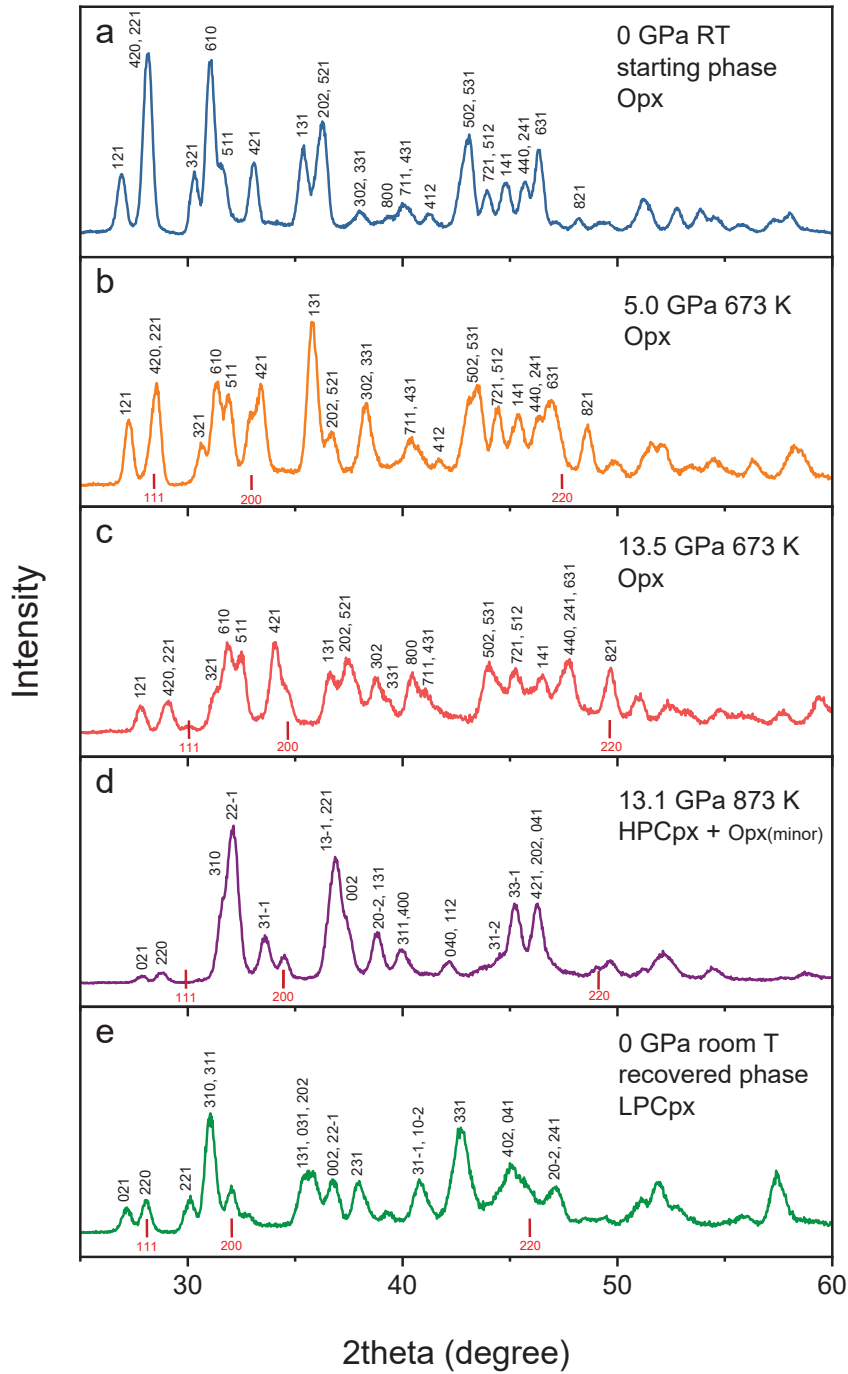


Figure 4

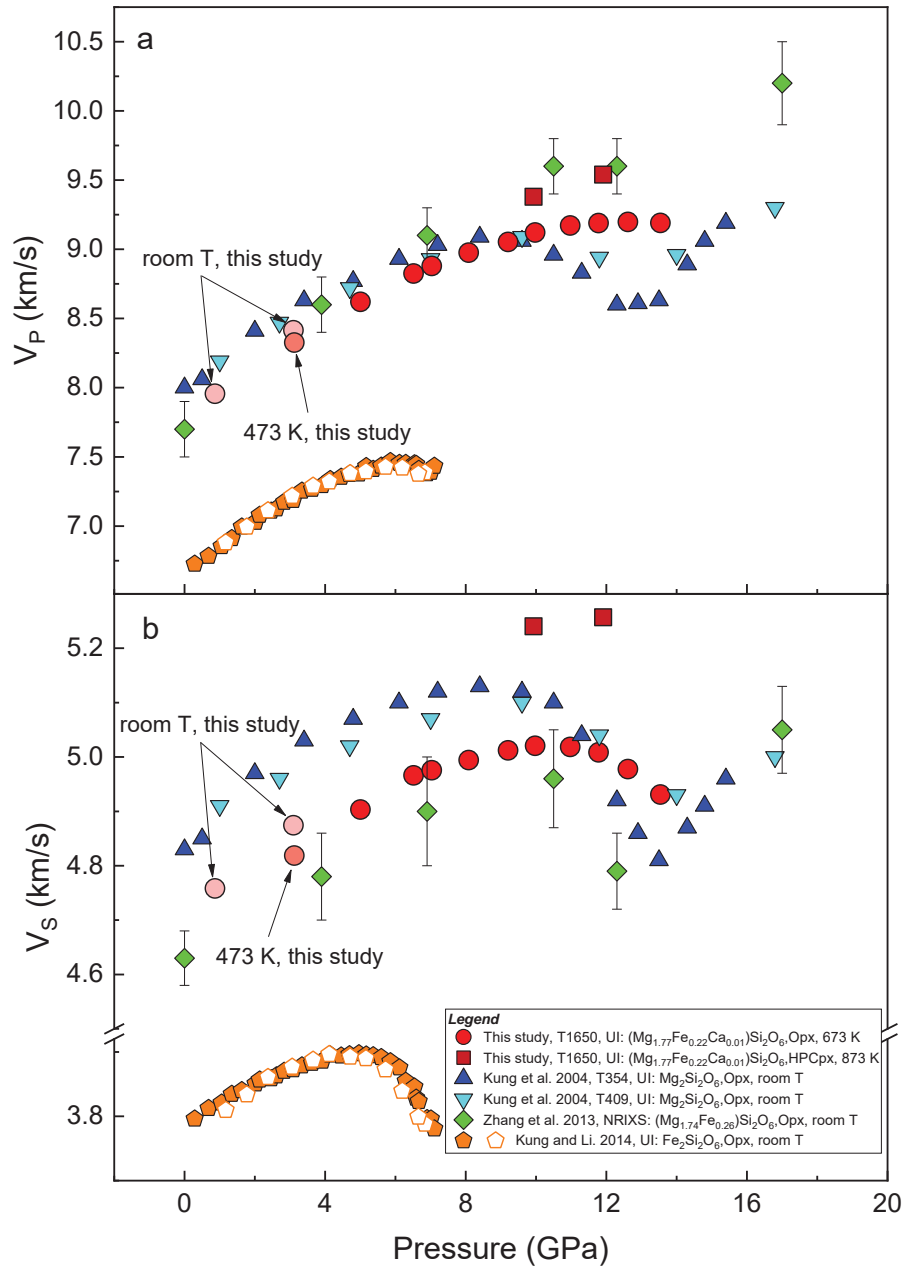


Figure 5

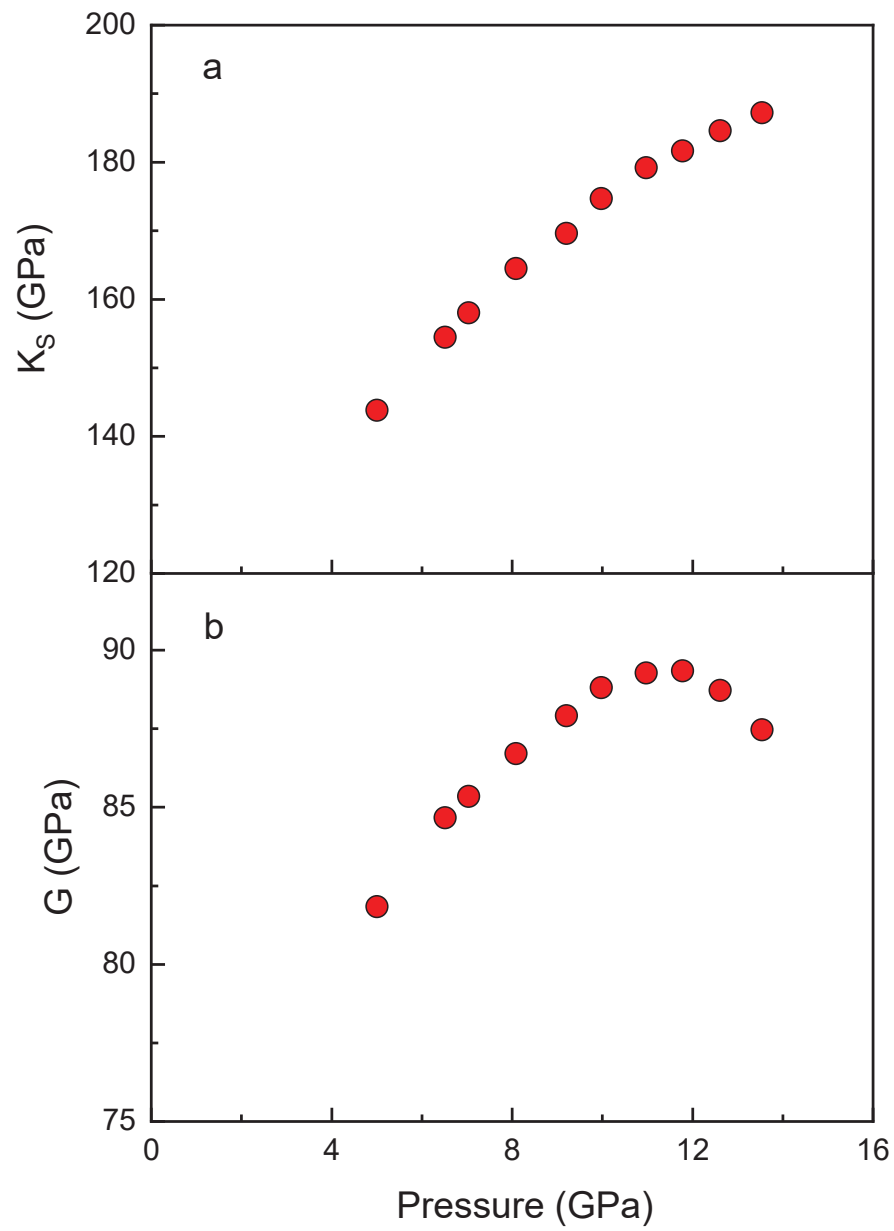


Figure 6